JACS
JOURNAL OF THE AMERICAN CHEMICAL SOCIETY
Article
Cite This: J. Am. Chem. Soc. XXXX, XXX, XXX−XXX
pubs.acs.org/JACS

Metal−Organic Frameworks Mediate Cu Coordination for Selective CO_2 Electroreduction

Dae-Hyun Nam,[†] Oleksandr S. Bushuyev,[†] Jun Li,[†,‡] Phil De Luna,[†,§] Ali Seifitokaldani,[†] Cao-Thang Dinh,[†] F. Pelayo García de Arquer,[†] Yuhang Wang,[†] Zhiqin Liang,[†] Andrew H. Proppe,[†,∥] Chih Shan Tan,[†] Petar Todorović,[†] Osama Shekhah,[⊥] Christine M. Gabardo,[‡] Jea Woong Jo,[†] Jongmin Choi,[†] Min-Jae Choi,[†] Se-Woong Baek,[†] Junghwan Kim,[†,¶] David Sinton,[‡] Shana O. Kelley,[∥,#] Mohamed Eddaoudi,[⊥] and Edward H. Sargent*[,†]

[†]Department of Electrical and Computer Engineering, University of Toronto, 10 King's College Road, Toronto, Ontario M5S 3G4, Canada

[‡]Department of Mechanical and Industrial Engineering, University of Toronto, 5 King's College Road, Toronto, Ontario M5S 3G8, Canada

[§]Department of Materials Science and Engineering, University of Toronto, 184 College Street, Toronto, Ontario M5S 3E4, Canada

[∥]Department of Chemistry, University of Toronto, 80 St. George Street, Toronto, Ontario M5S 3G4, Canada

[⊥]Division of Physical Sciences and Engineering, Advanced Membranes and Porous Materials Center, Functional Materials Design, Discovery and Development Research Group (FMD^3), King Abdullah University of Science and Technology (KAUST), Thuwal 23955-6900, Kingdom of Saudi Arabia

[#]Department of Pharmaceutical Sciences, Leslie Dan Faculty of Pharmacy, University of Toronto, 144 College Street, Toronto, Ontario M5S 3M2, Canada

Supporting Information

ABSTRACT: The electrochemical carbon dioxide reduction reaction (CO_2RR) produces diverse chemical species. Cu clusters with a judiciously controlled surface coordination number (CN) provide active sites that simultaneously optimize selectivity, activity, and efficiency for CO_2RR. Here we report a strategy involving metal−organic framework (MOF)-regulated Cu cluster formation that shifts CO_2 electroreduction toward multiple-carbon product generation. Specifically, we promoted undercoordinated sites during the formation of Cu clusters by controlling the structure of the Cu dimer, the precursor for Cu clusters. We distorted the symmetric paddle-wheel Cu dimer secondary building block of HKUST-1 to an asymmetric motif by separating adjacent benzene tricarboxylate moieties using thermal treatment. By varying materials processing conditions, we modulated the asymmetric local atomic structure, oxidation state and bonding strain of Cu dimers. Using electron paramagnetic resonance (EPR) and in situ X-ray absorption spectroscopy (XAS) experiments, we observed the formation of Cu clusters with low CN from distorted Cu dimers in HKUST-1 during CO_2 electroreduction. These exhibited 45% C_2H_4 faradaic efficiency (FE), a record for MOF-derived Cu cluster catalysts. A structure−activity relationship was established wherein the tuning of the Cu−Cu CN in Cu clusters determines the CO_2RR selectivity.

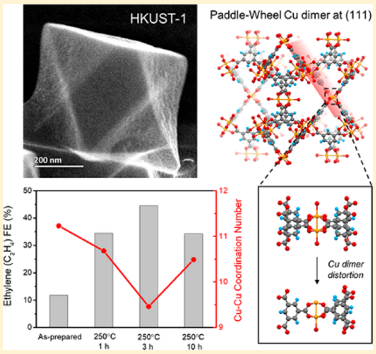

INTRODUCTION

The electrochemical carbon dioxide reduction reaction (CO_2RR) enables the storage of renewable energy in chemical form: it reduces CO_2 to products such as carbon monoxide (CO), methane (CH_4), ethylene (C_2H_4), formate ($HCOO^-$), ethanol (C_2H_5OH), and propanol (C_3H_7OH).[1] Copper (Cu) is capable of forming all of these chemicals, and efforts have been invested to increase the selectivity of value-added C2+ hydrocarbons. From a materials viewpoint, product selectivity is influenced by the surface structure,[2] oxidation states,[3] grain boundaries,[4] vacancies,[5] nanostructured morphology,[6] and pore size.[7]

The surface structure of materials is a critical factor in determining the reaction pathway.[8,9] The surface structure can be understood through the coordination number (CN), the number of nearest neighbor atoms. In CO_2RR, surface coordination control is crucial to CO_2 activation and intermediate stabilization, related ultimately to product selectivity. Theoretical

Received: June 18, 2018
Published: August 16, 2018

DOI: 10.1021/jacs.8b06407
J. Am. Chem. Soc. XXXX, XXX, XXX−XXX

studies have predicted product distributions by using Cu CN as a descriptor and calculating the energy of the intermediates: Cu-nanoparticle-covered Cu films with a low surface Cu CN show a higher C_2H_4 FE than an electropolished or sputtered uniform Cu surface due to high CHO* coverage.[2,10] Undercoordinated edge and corner sites on Cu surfaces are more active for C−C coupling.[11]

Compared to films, clusters and nanoparticles exhibit high surface-to-volume ratios and high turnover frequencies. As particle size decreases, surfaces tend to bind intermediates more strongly than on larger particle surfaces because of d-band narrowing.[9] It has been reported that hydrocarbon formation was inhibited, and H_2 and CO formation promoted, as the nanoparticle diameter decreased below 5 nm, a regime in which the ratio of low Cu−Cu CN (CN < 8) is high.[12] Therefore, to achieve high selectivity for C2 hydrocarbons, it is of interest to optimize the surface topography and the size of Cu clusters to influence intermediate reaction pathways.

Here we shift CO_2 electroreduction in Cu clusters toward multiple-carbon product generation by promoting undercoordinated Cu sites using metal−organic frameworks (MOFs). MOFs have received increased attention as a class of crystalline porous materials since they offer a platform to systematically control the metal site environment and porosity.[13,14] Controllable pore size/shape, high surface area, chemical tunability, Lewis acidity, and the open metal site of MOFs offer avenues to optimize selectivity, activity and efficiency.[15−18] Recently, it was reported that Cu clusters form from Cu ions in MOFs and organometallic catalysts during CO_2RR.[19] Previous authors have investigated the CO_2RR performance of Cu-based MOFs and organometallic catalysts, finding that a major CO_2RR product of HKUST-1 MOF was hydrogen (H_2).[19]

In this work, we distort the paddle-wheel structure of the Cu dimer in HKUST-1 MOF and apply this to modulate the surface structure of Cu clusters. Controlled calcination maintains overall MOF crystallinity while detaching carboxylate moieties from the Cu dimer in a stepwise manner. This process allows control over the Cu electronic configuration, local atomic structure, and bonding strain toward an asymmetric motif, as revealed using electron paramagnetic resonance (EPR). We utilized in situ X-ray absorption spectroscopy (XAS) to track the CN of Cu clusters during electrochemical CO_2RR cell operation. Undercoordinated site-promoted Cu clusters from the distorted Cu dimer, enabling us to increase the faradaic efficiency (FE) for ethylene (C_2H_4) from 10% to 45% while simultaneously decreasing H_2 generation to below 7%. This work provides insights into the utilization of MOFs as a mediator to modify the surface structure of Cu clusters for CO_2RR catalysts; and it suggests an important role for reticular chemistry in electrocatalysis.

RESULTS AND DISCUSSION

HKUST-1 Synthesis and Thermal Treatment. HKUST-1 ($C_{18}H_6Cu_3O_{12}$, $Cu_3(btc)_2{\cdot}xH_2O$, btc = benzene-1,3,5-tricarboxylate) was fabricated by reacting Cu nitrate ($Cu(NO_3)_2$) and trimesic acid ($C_9H_6O_6$, benzene-1,3,5-tricarboxylic acid) in methanol at room temperature.[20] The secondary building unit (SBU) of HKUST-1 is a paddle-wheel Cu dimer motif in which the distance between Cu metal nodes is 2.65 Å (Figure 1a).[21] Cu cations in the dimer are stabilized by the four oxygen atoms of four carboxylate groups. Cu acetate (CuAc, $Cu(CH_3COO)_2$) and HKUST-1 are each composed of a paddle-wheel Cu dimer as SBU; but with acetate pendant groups for CuAc as opposed to benzene tricarboxylates in HKUST-1. The benzene tricarboxylate groups of HKUST-1 generate a 3D structure with open pore sites (distance between benzene derivatives: 9 Å) and a periodic arrangement of Cu cations. The structure and elemental composition of as-prepared HKUST-1 in this work were investigated using scanning electron microscopy (SEM) and transmission electron microscopy (TEM) (Figure 1b−e). The HKUST-1 crystals are symmetric octahedra with flat faces. TEM bright field and high angle annular dark field (HAADF) images of as-prepared HKUST-1 before CO_2RR and before immersion in high pH solution confirm a homogeneous atomic distribution without agglomerated nanoparticles. The distribution of Cu, C, and O in TEM energy dispersive spectroscopy (EDS) mapping matched well with the shape of HKUST-1.

To modify the symmetric structure of the Cu dimer in HKUST-1, we attempted to increase the accessibility of the pentacoordinate Cu atomic center in the paddle-wheel SBU via thermal treatment. The calcination temperature was determined from the thermal behavior of HKUST-1 via thermogravimetric analysis (TGA) in air (Figure 1f). The weight percent of HKUST-1 (gray line) decreased to 75% at 200 °C which was attributed to dehydration of physically adsorbed water in the Cu SBU. When the temperature increased to above 300 °C, 45% mass was lost abruptly with a total enthalpy of 5965 J/g. The second thermogravimetric transition occurred at 307 °C with the derivative thermogravimetric (DTG) peak at 324 °C and differential scanning calorimetry (DSC) exothermic peak at 334 °C (blue and green line). Abrupt mass loss near 300 °C was attributed to MOF decomposition (organic combustion) under air.[22]

The phase and structural changes in HKUST-1 upon thermal treatment were characterized using X-ray diffraction (XRD) and SEM (Figure 1g, h). The XRD peak of as-prepared HKUST-1 matched well with the simulated XRD pattern.[23] When the sample was calcined at 250 °C, no phase and morphology changes in HKUST-1 were observed. However, when the temperature increased to 300°e, the XRD peaks for a mixture of Cu_2O and CuO were detected while the peaks for the HKUST-1 phase disappeared, indicating that the MOF phase was converted to crystalline Cu oxide phases. When we increased the temperature to 400 °C, pure CuO nanocrystals with a particle size of ∼100 nm were formed. Based on these results, 250 °C was chosen as the temperature at which to distort the symmetric Cu dimer by detaching carboxylate moieties for catalytic site activation (Figure 1g).

Materials Characterization vs Calcination Time. To modulate the degree of Cu dimer distortion, we kept the calcination temperature at 250 °C and varied the calcination isothermal time from 1 to 10 h. Figure 2 displays the effect of calcination isothermal time on the crystallinity and the bonding nature of HKUST-1. With longer calcination times, the color of HKUST-1 powder changed from light blue to dark green (Figure S2), while major XRD peaks for HKUST-1 were maintained even following 10 h thermal treatment (Figure 2a). Interestingly, the (111) plane peak began to disappear after 3 h calcination and the crystallinity of (200) plane decreased (peak intensity decrease) at the 10 h mark. 250 °C 1 h calcination shifted the overall diffraction pattern of HKUST-1 by 0.2° to a higher angle. However, as the calcination time increased to 3 and 10 h, the overall diffraction pattern of calcined HKUST-1 was shifted by 0.2 ∼ 0.3° to a lower angle compared to that of as-prepared HKUST-1 (Table S1).[24] Examination of the crystal structure of HKUST-1 revealed that a majority of the

DOI: 10.1021/jacs.8b06407
J. Am. Chem. Soc. XXXX, XXX, XXX−XXX

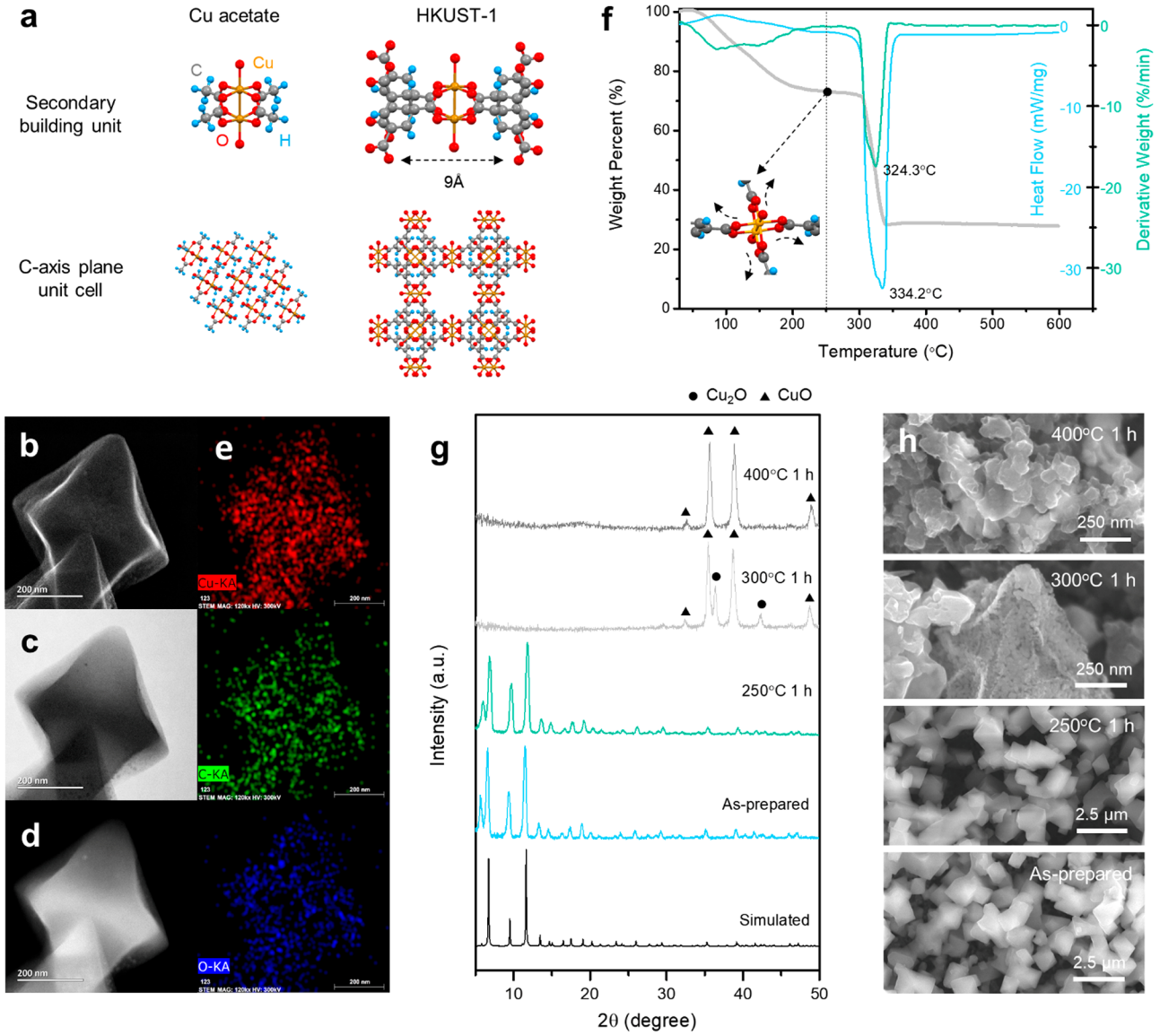

Figure 1. (a) Comparison of paddle-wheel structured HKUST-1 vs CuAc. Structural investigations of as-fabricated HKUST-1 by (b) SEM, (c) TEM bright field image, (d) TEM HAADF, and (e) TEM EDS. (f) TGA of HKUST-1 reveals optimal calcination temperature region where Cu dimer distortion is possible while maintaining the MOF structure. (g) XRD analysis to investigate the phase of HKUST-1 according to the calcination temperatures. (h) SEM images displaying the structures of HKUST-1 after the calcination.

paddle-wheel Cu dimers are positioned within the (111) plane (Figure 2b). Crystallinity loss of the (111) plane can be interpreted as structural distortion and ordering loss in the Cu dimers of the paddle-wheel SBU. Compared to HKUST-1, CuAc showed different phase transformation behavior upon calcination (Figure S4). The transition temperature for Cu oxide was lower than in HKUST-1 (300 → 250 °C). CuAc changed to Cu oxide when isothermally treated at a constant temperature.[25] Although each has a similar SBU, the control of crystallinity of a specific plane by calcination was possible only in HKUST-1. It also showed a more stable thermal behavior than CuAc.

Fourier transform infrared (FT-IR) spectroscopy and Raman analysis were performed to investigate the bonding features of organics in HKUST-1 using the isothermal time at 250 °C calcination. The FT-IR peak (Figure 2c) wave numbers for the symmetric vibration mode of C═O (1618 cm^{-1}), asymmetric vibration mode of O═C−O (1645, 1440 cm^{-1}), symmetric vibration mode of O═C−O (1370 cm^{-1}), vibration mode of C−O (1114 cm^{-1}), and vibration mode of phenyl (752, 729 cm^{-1}) were identical for both as-prepared and calcined samples (1, 3, 10 h).[26−28] The presence of major peaks for the C═C symmetric stretch of the benzene ring, C−H bend, and Cu−O stretch were observed in the Raman spectra of both as-prepared and calcined HKUST-1 (Figure 2d), confirming that the mainframe and organic bonding of HKUST-1 were maintained at 250 °C.[27,29,30] However, the relative peak intensity of the symmetric stretch in O═C−O decreased and asymmetric stretch of O═C−O disappeared as the calcination isothermal time increased from 1 to 10 h. Also, the full width at half-maximum (fwhm) associated with the C═C symmetric stretch of the benzene ring peak and C−H bend peak increased with decreasing peak intensity. Considering the atomic bonding nature of HKUST-1, we propose that carboxylic moieties are sequentially detached in the thermal activation process.

DOI: 10.1021/jacs.8b06407
J. Am. Chem. Soc. XXXX, XXX, XXX−XXX

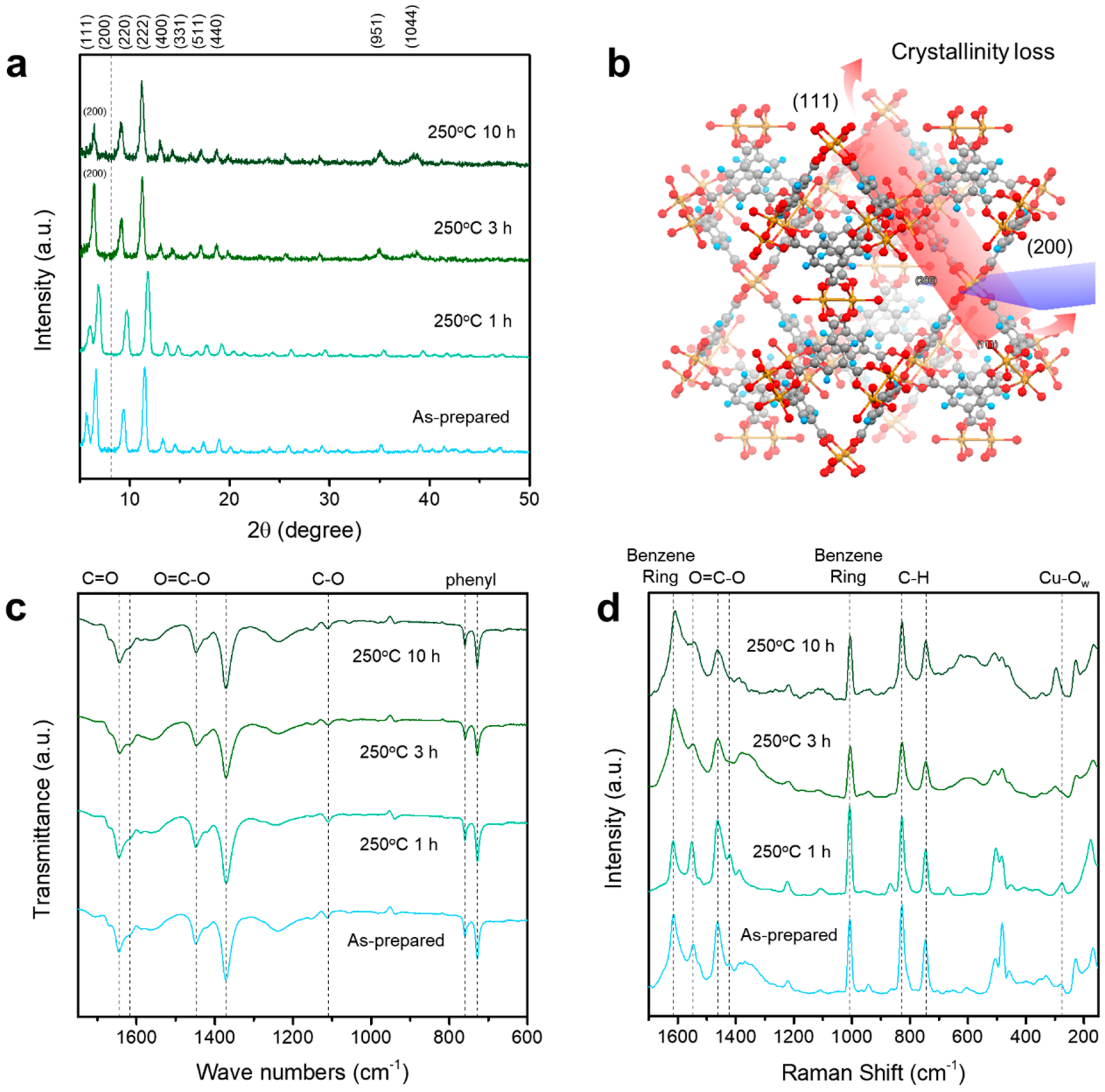

Figure 2. (a) XRD analysis of HKUST-1 calcined at 250 °C. As the isothermal time increases, the (111) plane crystallinity decreases. (b) Schematic of HKUST-1 to investigate the atomic arrangement in the (111) plane. (c) FT-IR analysis to relate HKUST-1 atomic bonding with isothermal calcination time at 250 °C. The spectra reveal that HKUST-1 structures are maintained following calcination. (d) Raman analysis to investigate the difference in the structural symmetry and bonding in HKUST-1 as a function of isothermal calcination time at 250 °C. The spectra indicate that carboxylate groups are detached from Cu after calcination.

HKUST-1 Cu Dimer Distortion. For detailed verification of Cu dimer atomic site modulation as a function of the degree of carboxylic moiety detachment, we used EPR, X-ray photoelectron spectroscopy (XPS), and SEM (Figure 3). EPR spectroscopy evaluates the unpaired electrons in atomic orbitals by detecting the magnetic moment of electron spin induced by a magnetic field (Zeeman effect).[31,32] The EPR signal and related parameters provide the information on the local atomic structure of a metal site: the unpaired electrons are directly affected by the atomic distance, bonding strain, and oxidation state. Cu 2+ exhibits a d-orbital electron configuration of d^9, spin state of S = 1/2, and axial EPR spectrum ($g_1 = g_2 < g_3$). The electronic structure of Cu dimers (oxidation state: 2+) in the paddle-wheel structures of HKUST-1 is in the antiferromagnetic singlet state (opposite spin direction of unpaired electron in d_{x2-y2} orbital) and the wave function is delocalized to the carboxylate group.[24,33]

The ground state of the electron configuration in as-prepared HKUST-1 was confirmed via EPR (Figure 3a). The Cu 2+ oxidation state of the dimer agrees with that determined using XPS (Figure 3b). SEM images of the as-prepared HKUST-1 show a uniform surface (Figure 3c). Following 1 h calcination at 250 °C, the EPR signal intensity of HKUST-1 increased and the peak became sharper compared to the as-prepared HKUST-1 (Figure 3d). Compared to the EPR signal of as-prepared HKUST-1, both the g_1 and g_2 factor increased (Table S2). Considering the identical XPS peak positions of Cu $2p_{1/2}$, $2p_{3/2}$, and the satellite for calcined vs as-prepared HKUST-1, the increase of the unpaired electron character in the Cu dimer can be explained by a change in the atomic distance and bonding strain (Figure 3e). The structure of HKUST-1 calcined at 250 °C for 1 h was similar to that of the as-prepared one (Figure 3f). Interestingly, as the isothermal time increased over 3 h, the EPR signal intensity and g_1 factor increased ($g_1 > g_2$) with decreased peak width compared to as-prepared and 1 h calcined HKUST-1 (Figure 3g, j). This EPR signal sharpening indicates the transition from antiferromagnetic to ferromagnetic states by increased unpaired electrons with parallel spin direction. This Cu d_{x2-y2} orbital energy level transition correlates with a change in the atomic environment

DOI: 10.1021/jacs.8b06407
J. Am. Chem. Soc. XXXX, XXX, XXX−XXX

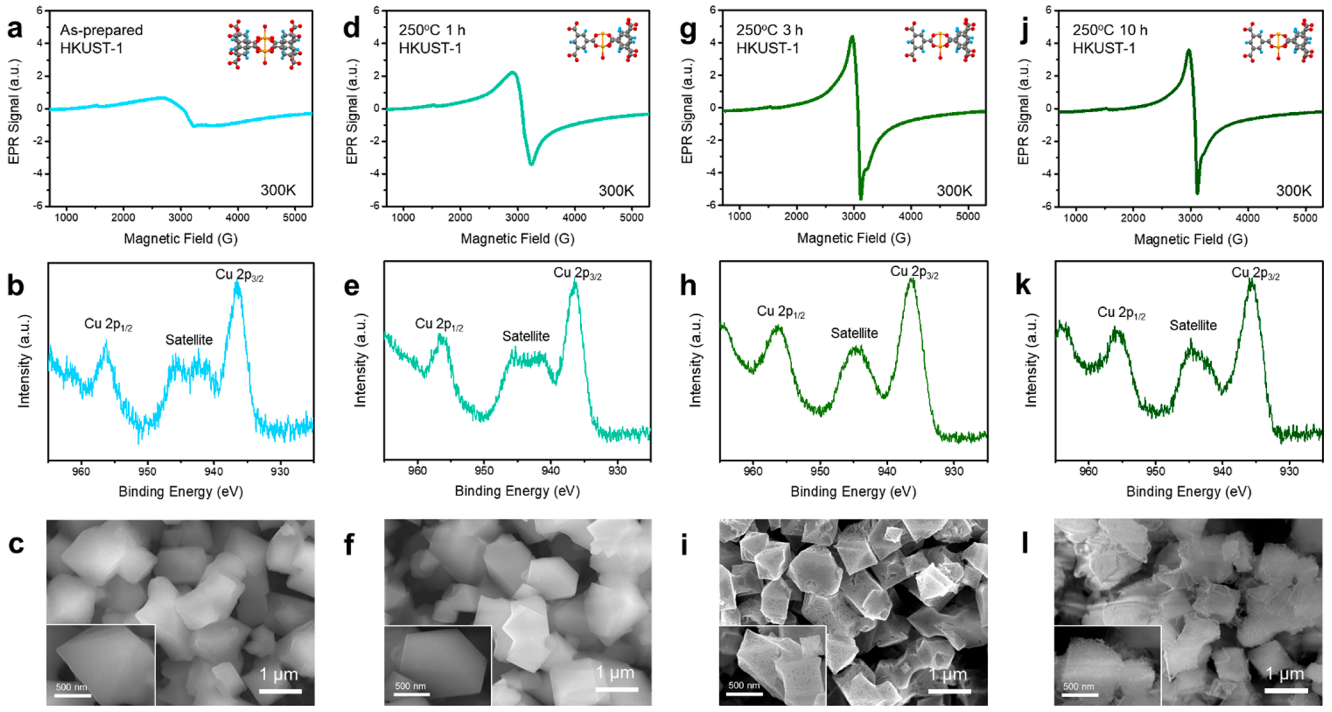

Figure 3. Effect of thermal calcination on the electron configuration and local atomic structure of paddle-wheel structured Cu dimer in HKUST-1. The distortion of symmetric Cu dimer toward the asymmetric structure was verified by EPR and XPS. Surface structure of HKUST-1 was investigated by SEM. They were compared according to the degree of thermal calcination. (a–c) As-prepared HKUST-1, (d–f) 250 °C 1 h calcined HKUST-1, (g–i) 250 °C 3 h calcined HKUST-1, and (j–l) 250 °C 10 h calcined HKUST-1.

to the asymmetric Cu dimer motif. The EPR peak intensity was higher in the 3 h than 10 h calcination. The shoulder at a magnetic field of 3250 G appeared and indicated structural distortion to asymmetric Cu dimer. The XPS peak width of Cu $2p_{1/2}$, $2p_{3/2}$ in the 3 and 10 h calcined HKUST-1 increased compared to that of the as-prepared and 1 h conditions. The shape of the Cu 2+ satellite peak changed to a single feature related with the "shake up" phenomenon (Figure 3h, k). This reveals that the Cu oxidation state in HKUST-1 was partially reduced from 2+ to 1+.[34,35] This Cu 1+ oxidation state generation can be observed in the Raman analysis. In Figure 2d, a Cu–O bonding peak of Cu 1+ around 600 cm^{-1} was observed in 250 °C 3 and 10 h calcined HKUST-1.[36] Also, the X-ray absorption near edge structure (XANES) of HKUST-1 reveals that the Cu oxidation state was reduced with increasing isothermal time of 250 °C calcination (Figure S5). Based on SEM images for surface structure investigation, we conclude that a porous structure was generated at the surface of HKUST-1 (Figure 3i, l). Overall, the isothermal time at 250 °C controls the local atomic structure and electron configuration of Cu atoms toward asymmetric paddle-wheel dimer. Since this EPR signal trend was not observed in CuAc, this Cu dimer distortion is specific to the HKUST-1 MOF (Figure S6).

In Situ XAS for Tracking Cu Cluster CN. In order to study the effect of Cu dimer distortion upon prethermal treatment on Cu cluster CN, we performed real-time catalyst characterization using in situ XAS under CO_2RR conditions (Figure 4). The dependence of the Cu oxidation states, bonding distance and CN of Cu–Cu and Cu–O on the thermal activation conditions were evaluated using XANES and extended X-ray absorption fine structure (EXAFS). We found that the Cu ion in HKUST-1 was reduced to metallic Cu clusters during CO_2RR testing conditions, consistent with recently reported results (Figures S7–S11).[19]

Interestingly, the in situ EXAFS data showed that the Cu–Cu CN of the Cu cluster was strongly dependent on the degree of Cu dimer distortion in HKUST-1 (Table S3). In as-prepared HKUST-1, the Cu dimer started to reduce to Cu clusters, and the Cu–Cu CN increased gradually toward 12 with decreasing Cu–O CN as the reaction continued to run (Figure 4a). The average Cu–Cu CN of the Cu cluster during the first 900 s reaction was 11.2 ± 0.6. In the 250 °C 1 h calcined HKUST-1, the average Cu–Cu CN of Cu cluster was reduced to 10.7 ± 0.7 (Figure 4b). The 250 °C 3 h calcined HKUST-1, which showed the asymmetric Cu dimer in EPR, formed the lowest average Cu–Cu CN of 9.5 ± 0.9 in the Cu cluster (Figure 4c). When the isothermal time of 250 °C calcination increased to 10 h, the Cu–Cu CN of Cu cluster increased to 10.5 ± 0.8 (Figure 4d). The formation of Cu clusters by the reduction of Cu ions in HKUST-1 and the change of Cu–Cu CN were confirmed using in situ XAS. In ex situ XAS and XPS experiments (Figures S12 and S13), the Cu oxidation number was the same 2+ before and after the reaction.[37] The ex situ XAS measurements of oxidized Cu suggest that the Cu is readily oxidized in air, which is consistent with the reactivity of small-sized clusters. There was no agglomeration of Cu clusters in SEM after the CO_2RR in 250 °C calcined HKUST-1 (Figures S14 and S15). Considering the in situ and ex situ characterization of HKUST-1, the Cu cluster size formed from the reduction of Cu dimer in HKUST-1 during CO_2RR was expected to be very small.[19] In the case of CuAc, it was found that the average Cu–Cu CN during CO_2RR increased continuously as a function of the degree of prethermal treatment (Figure S19). In contrast to the case of HKUST-1, agglomerated Cu was found in CuAc following CO_2RR (Figure S20).

DOI: 10.1021/jacs.8b06407
J. Am. Chem. Soc. XXXX, XXX, XXX–XXX

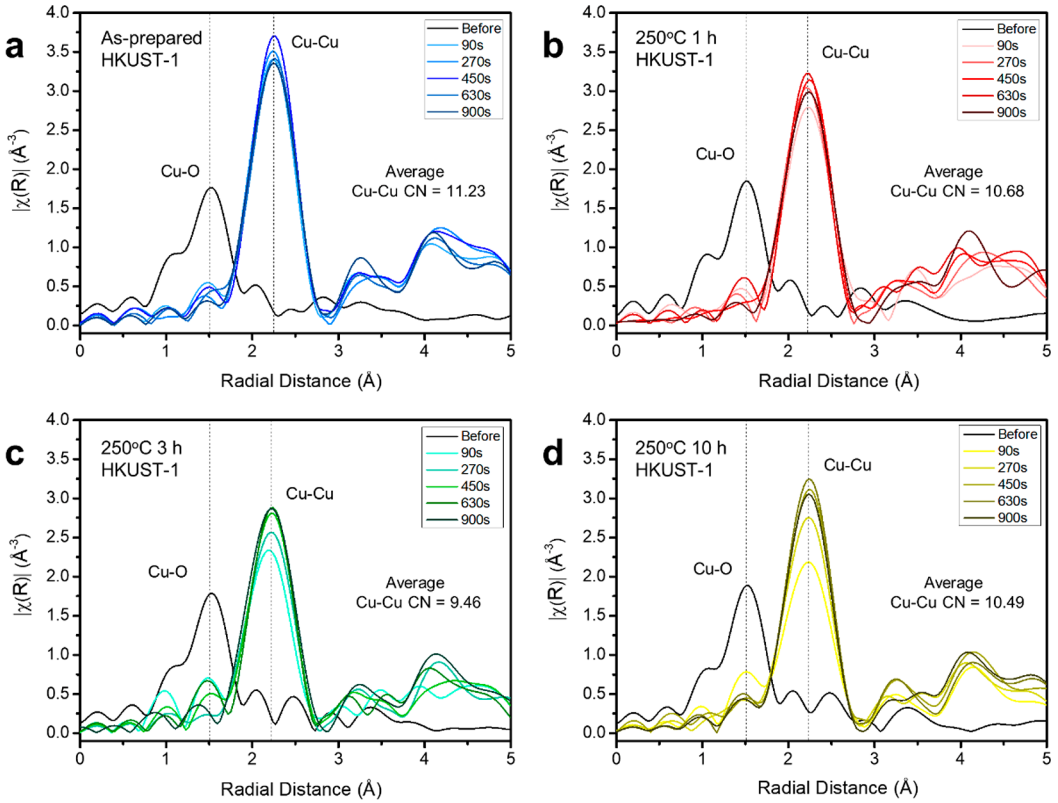

Figure 4. In situ EXAFS for tracking the real-time atomic structure of HKUST-1 derived Cu clusters during CO_2RR. EXAFS spectra were recorded according to the reaction time at the constant potential of −1.38 V vs RHE (non-iR corrected) in 1 M KOH; each spectrum was collected with a duration of 9 s. (a) As-prepared HKUST-1, (b) 250 °C 1 h calcined HKUST-1, (c) 250 °C 3 h calcined HKUST-1, and (d) 250 °C 10 h calcined HKUST-1.

In sum, for HKUST-1, the Cu dimer was distorted to the asymmetric motif by thermal treatment. As the Cu dimer was distorted, the Cu−Cu CN of Cu cluster remained low during CO_2RR. However, in CuAc, the Cu dimer was not distorted by prethermal treatment. Instead, as the degree of prethermal treatment increased, the Cu−Cu CN of Cu during CO_2RR increased. This behavior is due to accelerated Cu cluster agglomeration by prethermal treatment induced CH_3COO^- decomposition in CuAc.[38] We propose that the surface structure of Cu clusters is controlled only in HKUST-1 (Cu dimer with benzene tricarboxylates) and that the low Cu−Cu CN of Cu clusters from 250 °C calcined HKUST-1 may be explained by the regulating role of organic molecules in the MOF.[39]

CO_2RR Activity Evaluation. The electrochemical CO_2RR activity of HKUST-1 was evaluated in a flow cell configuration using 1 M KOH electrolyte.[40] Figure 5 shows the dependence of CO_2RR performance on the thermal activation process. In as-prepared HKUST-1, H_2 was generated with over 20% FE. The main product of CO_2RR was CO and the C_2H_4 FE was limited to 10%. Additionally, a relatively large amount of CH_4 was produced with the maximum FE of 15% (Figure 5a). The liquid products of HKUST-1 after CO_2RR included ethanol, acetate, and formate (Figures S25 and S26). In the 250 °C 1 h calcined HKUST-1, the C_2H_4 FE increased to 35% and H_2 FE decreased to 7% at all potentials (−0.64 to −0.99 V vs RHE). CH_4 FE was suppressed to less than 1% (Figure 5b). In the HKUST-1 calcined at 250 °C for 3 h with the lowest Cu−Cu CN of 9.5 ± 0.9, C_2H_4 FE was further enhanced up to 45% with the current density of 262 mA/cm^2 at −1.07 V vs RHE (Figure 5c). This value is the highest C_2H_4 FE reported among Cu organometallic and MOF based Cu catalysts to date (Table S5).[19,26,37,41−43] When the calcination time increased to 10 h, the C_2H_4 FE slightly decreased and H_2 FE increased slightly (Figure 5d). Promoting undercoordinated sites in Cu clusters increased C_2H_4 formation while suppressing H_2, CO, and CH_4 production. When the detachment degree of the benzene tricarboxylate group increased beyond the 250 °C 3 h condition, CO_2RR performance declined (Figure S27). The CO_2RR performance improvement by catalytic site activation in reticular chemistry-based materials is confirmed when one compares the performance of HKUST-1 and CuAc. The C_2H_4 FE of HKUST-1 was up to 20% higher than CuAc (Figure 5e).

To summarize: the distortion of the Cu dimer in HKUST-1 using thermal energy improved the CO_2RR performance of Cu clusters, and this enhanced performance was found to be closely related to maintaining a low Cu−Cu CN among the Cu clusters during the reaction.

■ CONCLUSION

In this work, we report a strategy to optimize the CO_2RR activity of Cu clusters by promoting undercoordinated Cu sites with the aid of a MOF. This performance tuning was realized by distorting the symmetric paddle-wheel Cu dimer of HKUST-1 to the asymmetric motif using thermal treatment. The Cu dimer distortion was achieved by separating the benzene tricarboxylate moieties. By varying the calcination isothermal time and keeping the calcination temperature at 250 °C, we controlled the distortion of HKUST-1 SBU while maintaining the HKUST-1 structure. The control of local atomic structure, bond strain, and electron configuration of

DOI: 10.1021/jacs.8b06407
J. Am. Chem. Soc. XXXX, XXX, XXX−XXX

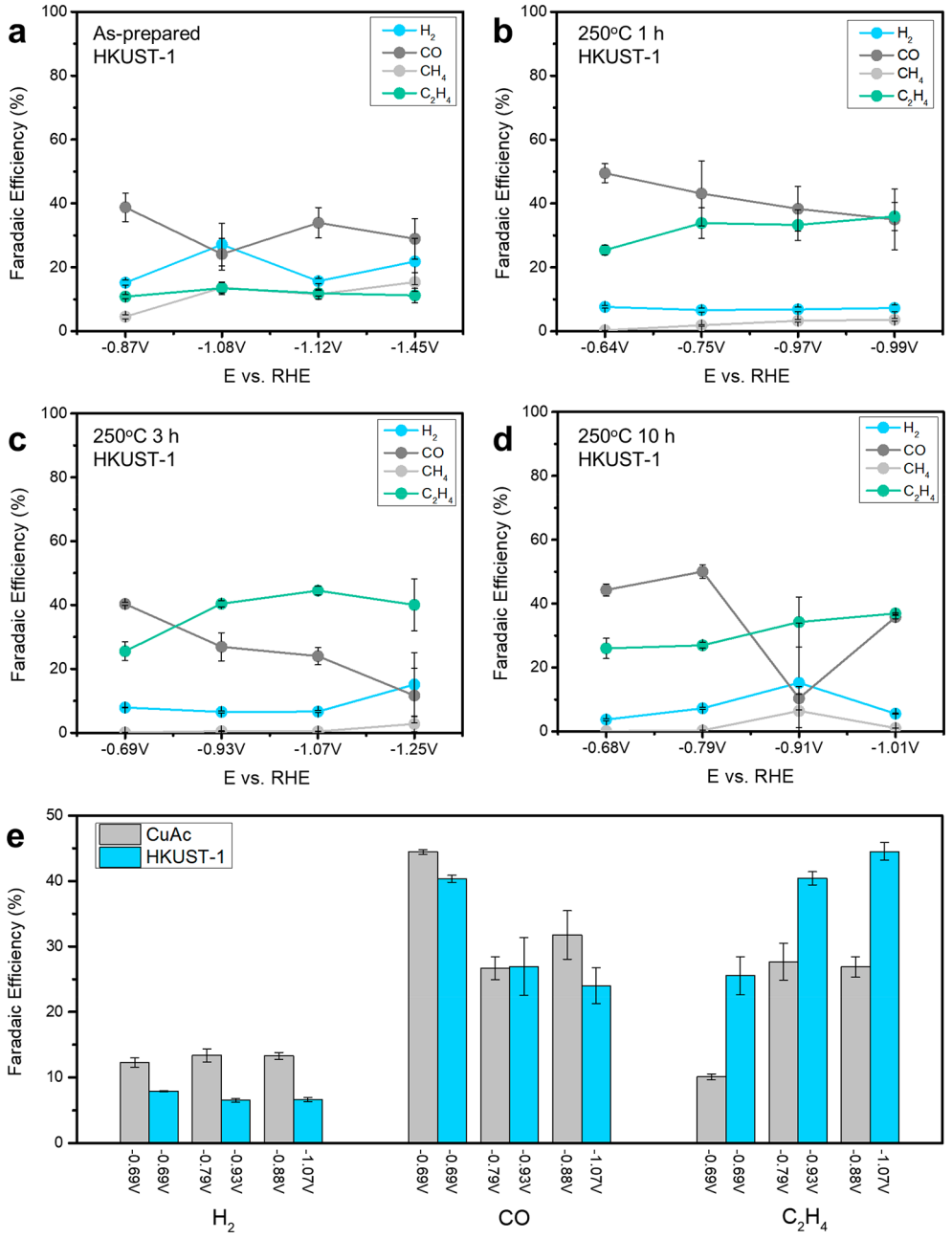

Figure 5. Investigation about the effect of Cu dimer distortion and coordination control on CO_2RR activity of HKUST-1 derived Cu clusters. CO_2 reduction product analysis at 1 M KOH operation of (a) as-prepared HKUST-1, (b) 250 °C 1 h calcined HKUST-1, (c) 250 °C 3 h calcined HKUST-1, and (d) 250 °C 10 h calcined HKUST-1. (e) Comparison of the CO_2RR activity between CuAc (200 °C 1 h calcined) derived Cu and HKUST-1 (250 °C 3 h calcined) derived Cu.

the asymmetric Cu dimer motif were closely related to maintaining a low Cu−Cu CN in MOF-derived Cu clusters during the reaction. Using this method, we improved MOF-derived CO_2RR performance to achieve a 45% C_2H_4 FE. The coordination control phenomenon is specific to the MOF, and the phase transformation during calcination, EPR signal, in situ XAS, and catalytic performance were appreciably unique for HKUST-1 vs CuAc. This work suggests additional avenues to explore metal−organic heterogeneous catalysts in CO_2RR.

EXPERIMENTAL SECTION

Cu Dimer Distorted HKUST-1 Fabrication. HKUST-1 ($C_{18}H_6Cu_3O_{12}$, $Cu_3(btc)_2{\cdot}xH_2O$, btc = benzene-1,3,5-tricarboxylate) was prepared by reacting Cu nitrate ($Cu(NO_3)_2$, Sigma-Aldrich) and trimesic acid ($C_9H_6O_6$, benzene-1,3,5-tricarboxylic acid, Sigma-Aldrich). Next, 1.82 g of Cu nitrate was dissolved in 50 mL methanol, and 0.875 g of trimesic acid was dissolved in 50 mL of methanol. After vortexing to produce a homogeneous solution, Cu nitrate solution was transferred to the trimesic acid solution. The mixed solution was stirred for 2 h at room temperature.[20] After stirring, a solution containing HKUST-1 was washed by centrifugation with methanol and vacuum-dried. Calcination proceeded at the furnace under ambient air. To investigate the phase after thermal treatment of HKUST-1, the calcination was performed at 250, 300, and 400 °C with a temperature ramping rate of 10 °C/min. After confirming the HKUST-1 crystalline phase remained at 250 °C, the isothermal time of calcination was varied to 1, 3, and 10 h to control the distortion of the symmetric Cu dimer in HKUST-1. CuAc

DOI: 10.1021/jacs.8b06407
J. Am. Chem. Soc. XXXX, XXX, XXX−XXX

($Cu(CH_3COO)_2{\cdot}H_2O$, M_w = 199.65 g/mol, Sigma-Aldrich) was used as a control sample. The calcination of CuAc was carried out at 200 and 250 °C to determine the temperature at which the CuAc crystalline phase would deteriorate. It was found that the CuAc crystal structure remained at a thermal treatment of 200 °C 1 h calcination.

Material Characterization. Thermal behavior of HKUST-1 according to the temperature was investigated by TG/DSC with a simultaneous thermal analyzer (NETZSCH STA 449 F3 Jupiter). The experiment was carried out in air flow (50 mL/min) at a heating rate of 10 °C/min using an initial HKUST-1 mass of 4.95 mg. The phase of HKUST-1 powder was verified by XRD with a Rigaku MiniFlex 600 diffractometer using Cu Kα radiation (λ = 1.5406 Å). XPS for Cu oxidation state (Cu 2p) investigation was carried out by using a Thermo Scientific Al Kα source XPS system with a spot size of 400 μm. SEM and TEM analysis for HKUST-1 structure characterization was carried out by using Hitachi FE-SEM S-5200 and Hitachi CFE-TEM HF3300 instruments. FT-IR was carried out by using a Thermo Scientific iS50 with the spectral range of 4600−50 cm^{-1}. Raman analysis was carried out by using a Renishaw microscope with the 535 nm laser. The power was 0.1% ans., and we scanned from 100 to 3200 cm^{-1}. Each scan was taken in 10 s, and we repeated the measurement six times. The spectrum is the average of six scans.

EPR Measurement. The local atomic structures of the paddlewheel Cu dimer in HKUST-1 and CuAc were measured by EPR. It was carried out by using a Bruker ECS-EMX X-band EPR spectrometer at the room temperature of 300 K. DPPH (2,2-diphenyl-1-picrylhydrazyl) was used for standardization of the peak position and intensity of the EPR signal. It has been measured by field sweep mode, and modulation amplitude was 4G. According to the order of as-prepared, 250 °C 1 h, 250 °C 3 h, and 250 °C 10 h calcined HKUST-1, the microwave frequency was 9.369, 9.372, 9.370, and 9.371 GHz, center field was 3326.5, 3329.9, 3328.85, and 3330.05 G, and sweep width was 5347.2, 5340.0, 5340.0, and 5340.0 G. The g factor and g strain were calculated by fitting the EPR signal with MATLAB based the EasySpin program ("pepper" function: calculation of field-swept solid-state cw EPR spectra for powders).

In Situ XAS Analysis. XAS measurements at the Cu K-edge were performed at the 9BM beamline of the Advanced Photon Source (APS, Argonne National Laboratory, IL). In situ XAS measurements were performed by using a custom flow cell in 1 M KOH electrolyte with CO_2 gas flowing from the backside of a gas diffusion layer.[40] In situ XANES and EXAFS scan data were collected during the cell operation mode of chronoamperometry at the potential of −2.4 V vs Ag/AgCl (−1.38 V vs RHE, non-iR corrected); same with the CO_2RR activity measurement condition.

Electrochemical CO_2 Reduction. CO_2RR activities of HKUST-1 and CuAc were measured by performing electrolysis in a flow cell. The cathode was composed of a HKUST-1 catalyst spray-coated gas diffusion layer (GDL, Sigracet), an anion exchange membrane, and a Pt foil as anode. The spray coating ink on GDL was made by dispersing HKUST-1 powder in Nafion + methanol solution followed by sonication. The deposited HKUST-1 mass per area was 0.56 mg/cm^2. CuAc was prepared on GDL with the same method of HKUST-1. 1 M KOH electrolyte was flowed in the cathode and anode chambers separately. CO_2 gas was flowed behind the GDL with a flow rate of 50 sccm. Chronoamperometry was performed using an electrochemical station (Autolab). The applied potentials of −2.4, −2.8, −3.2, and −3.6 V vs Ag/AgCl were tested with as-prepared, 250 °C 1 h, 250 °C 3 h, and 250 °C 10 h calcined HKUST-1. The electrode potentials were converted to RHE based on the following equation: $E_{RHE} = E_{Ag/AgCl} + 0.197\ V + 0.059 \times pH$. A resistance of 4.2 Ω was used to calculate the iR-correction. The collected gaseous products (H_2, CO, CH_4, C_2H_4) during CO_2RR were analyzed in 1 mL volumes by gas chromatography (PerkinElmer Clarus 600) with a thermal conductivity detector (TCD) and a flame ionization detector (FID). The number of moles of gas products was calculated from the gas chromatograph peak area. Liquid products were analyzed by ^1H NMR (Agilent DD2 500 spectrometer) in 10% D_2O water suppression mode, with dimethyl sulfoxide (DMSO) as an internal standard.

■ ASSOCIATED CONTENT

Supporting Information

The Supporting Information is available free of charge on the ACS Publications website at DOI: 10.1021/jacs.8b06407.

Detailed information about material characterization, EPR analysis, in situ XANES, EXAFS analysis, CO_2R activity measurement of HKUST-1 and CuAc (PDF)

■ AUTHOR INFORMATION

Corresponding Author

*ted.sargent@utoronto.ca

ORCID

Dae-Hyun Nam: 0000-0002-0871-1355
Phil De Luna: 0000-0002-7729-8816
Ali Seifitokaldani: 0000-0002-7169-1537
Cao-Thang Dinh: 0000-0001-9641-9815
F. Pelayo García de Arquer: 0000-0003-2422-6234
Andrew H. Proppe: 0000-0003-3860-9949
Osama Shekhah: 0000-0003-1861-9226
Christine M. Gabardo: 0000-0002-9456-6894
Jea Woong Jo: 0000-0001-8086-2644
Junghwan Kim: 0000-0003-3017-5330
David Sinton: 0000-0003-2714-6408
Shana O. Kelley: 0000-0003-3360-5359
Mohamed Eddaoudi: 0000-0003-1916-9837
Edward H. Sargent: 0000-0003-0396-6495

Present Addresses

¶Photo-electronic Hybrids Research Center, Korea Institute of Science and Technology (KIST), Seoul 02792, Korea

Notes

The authors declare no competing financial interest.

■ ACKNOWLEDGMENTS

This work was supported financially by the Natural Sciences and Engineering Research Council (NSERC) of Canada (RGPIN-2017-06477), the Ontario Research Fund: Research Excellence Program (ORF-RE-RE08-034). This publication is based upon work supported by the King Abdullah University of Science and Technology (KAUST) Office of Sponsored Research (OSR) under Award No. OSR-2017-CPF-3325-03. This research was supported by Basic Science Research Program through the National Research Foundation of Korea (NRF) funded by the Ministry of Education (2017R1A6A3A03004826). The authors thank Dr. T. P. Wu, Dr. Z. Finfrock, and Dr. L. Ma for technical support at the 9BM beamline of the Advanced Photon Source (Lemont, IL). C.M.G. acknowledges NSERC for funding in the form of a postdoctoral fellowship. P.D.L acknowledges NSERC for funding in the form of a Canada Graduate Scholar-Doctoral Scholarship.

■ REFERENCES

(1) Liu, M.; Pang, Y.; Zhang, B.; De Luna, P.; Voznyy, O.; Xu, J.; Zheng, X.; Dinh, C. T.; Fan, F.; Cao, C.; de Arquer, F. P. G.; Safaei, T. S.; Mepham, A.; Klinkova, A.; Kumacheva, E.; Filleter, T.; Sinton, D.; Kelley, S. O.; Sargent, E. H. *Nature* **2016**, *537*, 382−386.

(2) Zhao, Z.; Chen, Z.; Zhang, X.; Lu, G. *J. Phys. Chem. C* **2016**, *120*, 28125−28130.

(3) Mistry, H.; Varela, A. S.; Bonifacio, C. S.; Zegkinoglou, I.; Sinev, I.; Choi, Y.-W.; Kisslinger, K.; Stach, E. A.; Yang, J. C.; Strasser, P.; Cuenya, B. R. *Nat. Commun.* **2016**, *7*, 12123.

DOI: 10.1021/jacs.8b06407
J. Am. Chem. Soc. XXXX, XXX, XXX−XXX

(4) Feng, X.; Jiang, K.; Fan, S.; Kanan, M. W. *ACS Cent. Sci.* **2016**, *2*, 169−174.
(5) Zhuang, T.-T.; Liang, Z.-Q.; Seifitokaldani, A.; Li, Y.; De Luna, P.; Burdyny, T.; Che, F.; Meng, F.; Min, Y.; Quintero-Bermudez, R.; Dinh, C.-T.; Pang, Y.; Zhong, M.; Zhang, B.; Li, J.; Chen, P.-N.; Zheng, X.-L.; Liang, H.; Ge, W.-N.; Ye, B.-J.; Sinton, D.; Yu, S.-H.; Sargent, E. H. *Nat. Catal.* **2018**, *1*, 421−428.
(6) De Luna, P.; Quintero-Bermudez, R.; Dinh, C.-T.; Ross, M. B.; Bushuyev, O. S.; Todorović, P.; Regier, T.; Kelley, S. O.; Yang, P.; Sargent, E. H. *Nat. Catal.* **2018**, *1*, 103−110.
(7) Yang, K. D.; Ko, W. R.; Lee, J. H.; Kim, S. J.; Lee, H.; Lee, M. H.; Nam, K. T. *Angew. Chem., Int. Ed.* **2017**, *56*, 796−800.
(8) Calle-Vallejo, F.; Tymoczko, J.; Colic, V.; Vu, Q. H.; Pohl, M. D.; Morgenstern, K.; Loffreda, D.; Sautet, P.; Schuhmann, W.; Bandarenka, A. S. *Science* **2015**, *350*, 185−189.
(9) Zhang, X.; Liu, J.-X.; Zijlstra, B.; Filot, I. A. W.; Zhou, Z.; Sun, S.; Hensen, E. J. M. *Nano Energy* **2018**, *43*, 200−209.
(10) Tang, W.; Peterson, A. A.; Varela, A. S.; Jovanov, Z. P.; Bech, L.; Durand, W. J.; Dahl, S.; Norskov, J. K.; Chorkendorff, I. *Phys. Chem. Chem. Phys.* **2012**, *14*, 76−81.
(11) Hahn, C.; Hatsukade, T.; Kim, Y.-G.; Vailionis, A.; Baricuatro, J. H.; Higgins, D. C.; Nitopi, S. A.; Soriaga, M. P.; Jaramillo, T. F. *Proc. Natl. Acad. Sci. U. S. A.* **2017**, *114*, 5918−5923.
(12) Reske, R.; Mistry, H.; Behafarid, F.; Roldan Cuenya, B.; Strasser, P. *J. Am. Chem. Soc.* **2014**, *136*, 6978−6986.
(13) Eddaoudi, M.; Kim, J.; Rosi, N.; Vodak, D.; Wachter, J.; O'Keeffe, M.; Yaghi, O. M. *Science* **2002**, *295*, 469−472.
(14) Liu, G.; Chernikova, V.; Liu, Y.; Zhang, K.; Belmabkhout, Y.; Shekhah, O.; Zhang, C.; Yi, S.; Eddaoudi, M.; Koros, W. J. *Nat. Mater.* **2018**, *17*, 283−289.
(15) Diercks, C. S.; Liu, Y.; Cordova, K. E.; Yaghi, O. M. *Nat. Mater.* **2018**, *17*, 301−307.
(16) Kornienko, N.; Zhao, Y.; Kley, C. S.; Zhu, C.; Kim, D.; Lin, S.; Chang, C. J.; Yaghi, O. M.; Yang, P. *J. Am. Chem. Soc.* **2015**, *137*, 14129−14135.
(17) Diercks, C. S.; Lin, S.; Kornienko, N.; Kapustin, E. A.; Nichols, E. M.; Zhu, C.; Zhao, Y.; Chang, C. J.; Yaghi, O. M. *J. Am. Chem. Soc.* **2018**, *140*, 1116−1122.
(18) Lin, S.; Diercks, C. S.; Zhang, Y.-B.; Kornienko, N.; Nichols, E. M.; Zhao, Y.; Paris, A. R.; Kim, D.; Yang, P.; Yaghi, O. M.; Chang, C. J. *Science* **2015**, *349*, 1208−1213.
(19) Weng, Z.; Wu, Y.; Wang, M.; Jiang, J.; Yang, K.; Huo, S.; Wang, X.-F.; Ma, Q.; Brudvig, G. W.; Batista, V. S.; Liang, Y.; Feng, Z.; Wang, H. *Nat. Commun.* **2018**, *9*, 415.
(20) Wu, R.; Qian, X.; Yu, F.; Liu, H.; Zhou, K.; Wei, J.; Huang, Y. *J. Mater. Chem. A* **2013**, *1*, 11126−11129.
(21) Chui, S. S.-Y.; Lo, S. M.-F.; Charmant, J. P. H.; Orpen, A. G.; Williams, I. D. *Science* **1999**, *283*, 1148−1150.
(22) Nam, D.-H.; Lee, S.; Lee, Y.-J.; Jo, J.-H.; Yoon, E.; Yi, K.-W.; Lee, G.-D.; Joo, Y.-C. *Adv. Mater.* **2017**, *29*, 1702958.
(23) Yakovenko, A. A.; Reibenspies, J. H.; Bhuvanesh, N.; Zhou, H.-C. *J. Appl. Crystallogr.* **2013**, *46*, 346−353.
(24) Todaro, M.; Buscarino, G.; Sciortino, L.; Alessi, A.; Messina, F.; Taddei, M.; Ranocchiari, M.; Cannas, M.; Gelardi, F. M. *J. Phys. Chem. C* **2016**, *120*, 12879−12889.
(25) Lin, Z.; Han, D.; Li, S. *J. Therm. Anal. Calorim.* **2012**, *107*, 471−475.
(26) Albo, J.; Vallejo, D.; Beobide, G.; Castillo, O.; Castaño, P.; Irabien, A. *ChemSusChem* **2017**, *10*, 1100−1109.
(27) Dhumal, N. R.; Singh, M. P.; Anderson, J. A.; Kiefer, J.; Kim, H. J. *J. Phys. Chem. C* **2016**, *120*, 3295−3304.
(28) Toyao, T.; Liang, K.; Okada, K.; Ricco, R.; Styles, M. J.; Tokudome, Y.; Horiuchi, Y.; Hill, A. J.; Takahashi, M.; Matsuoka, M.; Falcaro, P. *Inorg. Chem. Front.* **2015**, *2*, 434−441.
(29) Todaro, M.; Alessi, A.; Sciortino, L.; Agnello, S.; Cannas, M.; Gelardi, F. M.; Buscarino, G. *J. Spectrosc.* **2016**, *2016*, 1.
(30) Prestipino, C.; Regli, L.; Vitillo, J. G.; Bonino, F.; Damin, A.; Lamberti, C.; Zecchina, A.; Solari, P. L.; Kongshaug, K. O.; Bordiga, S. *Chem. Mater.* **2006**, *18*, 1337−1346.
(31) Ahmad, R.; Kuppusamy, P. *Chem. Rev.* **2010**, *110*, 3212−3236.
(32) Junk, M. J. N. Electron Paramagnetic Resonance Theory BT - Assessing the Functional Structure of Molecular Transporters by EPR Spectroscopy; Junk, M. J. N., Ed.; Springer: Berlin, Heidelberg, 2012; pp 7−52.
(33) Hendon, C. H.; Walsh, A. *Chem. Sci.* **2015**, *6*, 3674−3683.
(34) St. Petkov, P.; Vayssilov, G. N.; Liu, J.; Shekhah, O.; Wang, Y.; Wöll, C.; Heine, T. *ChemPhysChem* **2012**, *13*, 2025−2029.
(35) Biesinger, M. C.; Lau, L. W. M.; Gerson, A. R.; Smart, R. S. C. *Appl. Surf. Sci.* **2010**, *257*, 887−898.
(36) Gan, Z. H.; Yu, G. Q.; Tay, B. K.; Tan, C. M.; Zhao, Z. W.; Fu, Y. Q. *J. Phys. D: Appl. Phys.* **2004**, *37*, 81−85.
(37) Weng, Z.; Jiang, J.; Wu, Y.; Wu, Z.; Guo, X.; Materna, K. L.; Liu, W.; Batista, V. S.; Brudvig, G. W.; Wang, H. *J. Am. Chem. Soc.* **2016**, *138*, 8076−8079.
(38) Manthiram, K.; Beberwyck, B. J.; Alivisatos, A. P. *J. Am. Chem. Soc.* **2014**, *136*, 13319−13325.
(39) Liu, P.; Qin, R.; Fu, G.; Zheng, N. *J. Am. Chem. Soc.* **2017**, *139*, 2122−2131.
(40) Dinh, C.-T.; Burdyny, T.; Kibria, M. G.; Seifitokaldani, A.; Gabardo, C. M.; García de Arquer, F. P.; Kiani, A.; Edwards, J. P.; De Luna, P.; Bushuyev, O. S.; Zou, C.; Quintero-Bermudez, R.; Pang, Y.; Sinton, D.; Sargent, E. H. *Science* **2018**, *360*, 783−787.
(41) Kusama, S.; Saito, T.; Hashiba, H.; Sakai, A.; Yotsuhashi, S. *ACS Catal.* **2017**, *7*, 8382−8385.
(42) Kung, C.-W.; Audu, C. O.; Peters, A. W.; Noh, H.; Farha, O. K.; Hupp, J. T. *ACS Energy Lett.* **2017**, *2*, 2394−2401.
(43) Qiu, Y.-L.; Zhong, H.-X.; Zhang, T.-T.; Xu, W.-B.; Su, P.-P.; Li, X.-F.; Zhang, H.-M. *ACS Appl. Mater. Interfaces* **2018**, *10*, 2480−2489.

DOI: 10.1021/jacs.8b06407
J. Am. Chem. Soc. XXXX, XXX, XXX−XXX